A green and facile fabrication of rGO/FEVE nanocomposite coating for anti-corrosion application

Luyan Shen[1], He Chen[1], Chunhong Qi[1], Qiang Fu[1, 2], Zhiyuan Xiong[3], Youyi Sun[1*], Yaqing Liu[1]

1.Shanxi Province Key Laboratory of Functional Nanocomposites, North University of China, Taiyuan 030051, P.R.China.

2.School of Civil and Environmental Engineering, University of Technology Sydney, Ultimo NSW 2007, Australia.

3. Department of Chemical and Bio-molecular Engineering, The University of Melbourne, Victoria 3010, Australia.

Abstract: A facile process was developed to fabricate rGO/fluoroethylene vinyl ether (FEVE) nanocomposite coating for anti-corrosion application. Dry rGO modified with PS sphere were prepared with good re-dispersibility and directly added into FEVE organic paint, forming a rGO/FEVE nanocomposite coating. Furthermore, the effect of modified rGO on structure and properties of composite coating was investigated in detail. It was found that the composite coating (1.5wt%) displayed best mechanical properties (e.g. adhesion strength of 14 MPa) and anti-corrosive performance (e.g. corrosive current density of 7.6×10^{-12}A/cm^2) comparing with other composite coating based on rGO. This work thus provides a facile and environmentally friendly method to prepare novel nanocomposite coatings with enhanced performance for various practical applications.

Keywords: FEVE coating, PS-PVP@rGO, good dispersion, mechanical property, anti-corrosion.

Responding author: Fax: 86-351-3559669

E-mail address: syyi@pku.edu.cn (YY Sun)

1. Introduction

Reduced graphene oxide (rGO)-based polymer nanocomposites have attracted lots of attentions for protection metals from corrosion due to their unique properties, such as high surface area, nanometric thickness, impermeable against oxygen and water [1-3]. Solution mixing is arguably the simplest and most effective method to prepare rGO-based polymer nanocomposites [4-5]. In general, this method involves mixing colloidal suspension of rGO with polymer solutions via shear-mixing or stirring. Most of previous research works focuses on the preparation of rGO-based polymer nanocomposites by mixing rGO and water-soluble polymers in aqueous media because modified rGO nanosheets usually display good dispersibility in aqueous solution [6-13]. However, the waterborne polymer coatings suffer insufficient anti-corrosion performance compared to the coatings made of hydrophobic polymers, such as epoxy resins, polyurethane, silicone-acrylate resin, fluoroethylene vinyl ether (FEVE) resin and rubbers, which are dissolved in various organic solvents. Therefore, in order to further enhance the anti-corrosion performance of rGO/polymer composites, it is necessary to improve the dispersibility of rGO nanosheets in organic solvents to provide a uniform rGO/polymer suspension. Generally, there are two approaches to improve the dispersibility of rGO nanosheets in organic solvents. One method is to remove the water in the modified rGO nanosheets *via* thermal drying, followed by re-dispersing in organic solvents. The disadvantage of this method is that irreversible aggregation is easily formed during the thermal drying process. Another method is to wash the modified rGO nanosheets with organic solvents to completely remove water. Then the modified rGO nanosheets were dispersed in organic solvent under ultrasonication. In this method, the rGO nanosheets show good re-dispersibility in organic solvent, however it involves multi-step purification and a large number of organic solvents are used, restricting its practical application. Therefore, it is still a challenge to develop a "green", versatile and cost-effective method for preparing rGO and oil-soluble polymer nanocomposite coatings. FEVE resin has been widely applied in anti-corrosive industry due to its excellent resistance to weather, acid rain, salt fog and chemicals [14-16]. FEVE resin can only be dissolved in organic solvents, which brings difficulties to the preparation of rGO/FEVE nanocomposite coatings for anti-corrosion applications.

In this paper, a novel method for the preparation of rGO/FEVE nanocomposite coatings was developed. The rGO nanosheets was modified with polystyrene (PS) nanospheres to reduce *van der* Waals interaction between rGO nanosheets, suppressing irreversible aggregate of dry rGO nanosheets. At the same time, the attached PS can provide enhanced re-dispersibility of rGO in organic solvent. Thereafter, the dry modified rGO nanosheets were directly added into the FEVE solution to afford a stable and uniform mixture, which can be applied in real anti-corrosion industry.

2. Experimental

2.1 Materials

Graphene oxide aqueous solution (1 mg/mL) was purchased from Tangshan Jianhua Technology Development Co., Ltd. Hydrazine hydrate and polyvinyl pyrrolidone (PVP) were purchased from Tianjin guangfu technology development Co., Ltd. $NaHSO_4$, $K_2S_2O_8$ and styrene (St) were purchased from Aladdin Industrial Corporation. All reagents except St were used as received without further purification. St was washed with 5.0% NaOH solution to remove the phenolic inhibitors. Fluoro resin was purchased from Shan Dong Ying Qiang New Materials Technology Co., Ltd. The steel panels (Q235, 120mm×50mm×0.2 mm) were purchased from Biuged Laboratory Instruments (Guangzhou) Co., Ltd., Guangzhou, China.

2.2 Preparation of PS-PVP@rGO/FEVE nanocomposite coating

The PS-PVP@rGO/FEVE nanocomposite coatings were prepared by a two-step method as shown in following. Firstly, 0.15 g PVP was dissolved in 100 mL graphene oxide (GO) aqueous solution under ultrasonication for 5 min to form a GO/PVP (PVP@GO) suspension. And then 0.05g $NaHSO_4$, 0.05g $K_2S_2O_8$ and 2.5g St were added into above aqueous solution, which was heated to 70℃ for 6 hours under nitrogen protection. The PS-PVP@GO was further reduced by hydrazine hydrate (40 wt%) at 80℃ for 2 hours to afford the PS-PVP@rGO, followed by a spray-drying process to remove water. Secondly, the dry PS-PVP@rGO nanosheets (0, 0.5, 1, 1.5 and 2 wt%), FEVE resin (40wt%) and curing agent were mixed in xylene under mechanically stirring. the mixtures were coated on the surfaces of Q235 carbon steel substrates via spray-coating. The composite coatings were cured at room temperature for 48 hours, forming a uniform nanocomposite coating.

2.4 Measurements and characterization

Fourier transform infrared spectrometer (FT-IR) (Thermo Nicolet 360) was carried to examine the different chemical bonds.

The Raman spectroscopy was characterized by a LabRAM HR-800 Raman spectrometer with an incident laser beam of 532.4 nm (Horiba Scientific).

Scanning electron microscopy (SEM) images were acquired using Su-8010 electron microscopy (HITACHI Japan).

The knife-scratch and pull-off tests were carried out according to ASTM D 3359-09 and GB/T 5210-2006 respectively to determine the adhesion strength of the coatings to the substrate.

The falling weight tests were conducted to measure the impact resistance according to GB/T1732-1993.

2.5 Electrochemical measurements

All the electrochemical corrosion measurements were performed with a standard three-electrode in electrochemical workstation (CHI660C, Chenhua, Shanghai) at room temperature. The uncoated or coated carbon steels were applied as the working electrode. The saturated calomel electrode (SCE) and Pt wire were used as the reference and counter electrode, respectively. All tests were conducted in a corrosive medium (3.5 wt% sodium chloride solution). The working electrode was immersed in the corrosive medium for 1 hour to ensure a steady state before the measurements. The corrosion current density (I_{corr}) and corrosion potential (E_{corr}) were calculated by Tafel method. The polarization resistance (R_p) was determined by the following equation [16].

$$R_p = \frac{b_a \times b_c}{2.303 I_{corr}\left(b_a + b_c\right)}$$

Where b_a and b_c are the slopes of the anodic and cathodic Tafel plots, respectively.

The corrosion rate (V_{corr}) is calculated from the following equation [17]:

$$V_{corr} = \frac{A I_{corr}}{n \rho F} \times 87600\left(mm / year\right)$$

Where A is the molecular weight of metal (55.85 g/mol), n is the chemical valence of iron (2), ρ is the density of iron (7.85 g/cm^3) and F is the Faraday constant (96485 C/mol).

3. Result and discussion

The synthesis of dry PS-PVP@rGO powders with good re-dispersibility in organic solvents is a key challenge for the preparation of uniform rGO/FEVE nanocomposite coatings. Generally, dry pure rGO nanosheets tend to form irreversible aggregates due to their large surface area and strong *van der* Waals interaction [18]. Therefore, dry pure rGO nanosheets are difficult to re-disperse in water or other organic solvents, even modified with organic molecules [13]. It is known that *van der* Waals interactions decrease with increasing in the *d*-spacing between nanosheets [19]. From this respective, enlarging the d-spacing is an effective way to suppress the *van der* Waals interactions and prevent the formation of irreversible rGO aggregate. In this study, PS nanospheres were coated on the surface of rGO under assistance of PVP to extend the *d*-spacing, thereby reducing the *van der* Waals interaction between dry rGO nanosheets, and enhancing the re-dispersibility of dry PS-PVP@rGO nanosheets in organic solvents.

The formation and structure of PS-PVP@rGO was confirmed and characterized by the IR, Raman, SEM and TEM images. Fig.1A shows the IR spectra of pure rGO and PS-PVP@rGO product. For the pure rGO sample, there was only one obvious absorption peak at 1637cm^{-1}, which was assigned to C=O of rGO [20]. For the PS-PVP@rGO sample, there presented some new absorption peaks, which were assigned to PVP and PS. For example, the absorption peaks at 1650 cm^{-1} and 1281 cm^{-1} were assigned to C=O and C-N vibrations of PVP, respectively [20]. The absorption peaks at 1601 cm^{-1} and 1492 cm^{-1} were assigned to (C=C) stretching vibration of benzene ring in PS [21]. The absorption peaks at 3081 cm^{-1}, 3059 cm^{-1} and 3021 cm^{-1} were assigned to the C-H stretching vibration of benzene ring in PS [22]. The result indicated that the products contained both PS and PVP components. In addition, it was found that it showed similar IR spectra for the PS-PVP@rGO before and after dispersing in xylene. The result indicated that PS was adsorbed on surface of rGO under assistant of PVP. The Raman spectrum of PS-PVP@rGO was also characterized as shown in Fig.1B. It clearly showed two absorption peaks at 1308.9 and 1595 cm^{-1}, which were assigned to D and G band of rGO, respectively, suggesting that the product contained rGO component [5]. These results confirmed the formation of PS-PVP@rGO. Fig.1C and Fig1D shows the SEM images of pure rGO and PS-PVP@rGO, respectively. Pure rGO and PS-PVP@rGO sample both clearly showed sheet-like materials. In a comparison, the pure rGO showed smooth surface, while PS-PVP@rGO showed roughness surface, which was attributed to covered PS nanospheres. Above results were further confirmed by the TEM images. For the rGO sample, it clearly showed transparent and fold film, which was assigned to rGO nanosheets (in Fig.1E). After covering with PS nanospheres, there was obvious some nanospheres on surface of rGO as shown in Fig.1F. This result further demonstrated the successful preparation of rGO modified with PS nanospheres via *in-situ* polymerization. Moreover, the dry PS-PVP@rGO nanosheets could be re-dispersed in xylene, affording a stable suspension for more than 6 months as shown in inset of Fig.1B. The result confirmed the formation of PS-PVP@rGO nanosheets with good dispersion.

Fig.1.

The obtained dry PS-PVP@rGO nanosheets could be directly mixed with FEVE in xylene to form rGO/FEVE nanocomposite coatings. The micro-structures of rGO/FEVE nanocomposite coatings with different contents of PS-PVP@rGO were characterized by the SEM and optical microscopical images as shown in Fig.2. The thickness of formed nanocomposite coating was about 100.0μm as shown in Fig.2A. In addition, all samples showed a smooth surface and few pinholes as shown in Fig.2B-F. However, due to the curing shrinkage and solvent evaporation of all samples, some cracks were observed. When the content of PS-PVP@rGO was less than 1.5wt%, we observed fewer cracks, which was attributed to the uniform distribution of PS-PVP@rGO in FEVE resin matrix. The introduction of PS-PVP@rGO could improve the mechanical properties and effectively reduce the curing shrinkage of coating. In contrast, when the content (2.0wt%) of PS-PVP@rGO was higher than 1.5wt%, we observed more cracks due to the poor compatibility between PS and FEVE, resulting in phase separation. Furthermore, no aggregates were observed in the polymer nanocomposite, which was rarely reported in previous literature. These results further demonstrated the uniform distribution of rGO in FEVE matrix, leading to enhanced barrier property of rGO/FEVE nanocomposite coatings.

Fig.2.

The adhesion ability of rGO/FEVE nanocomposite coating on metal substrate was firstly measured by knife-scratch and pull-off tests as shown in Fig.3. The grades 5B to 0B are generally used to evaluate the adhesion ability according to ASTM D3359, whereas 5B and 0B represents the highest and lowest adhesion ability, respectively [22]. Fig.3A-E show the images of cross-cut tests performed on coatings with different contents of PS-PVP@rGO. No obvious desquamation was observed in all samples, which means 5B grade coatings were formed. The adhesion strength was further studied by pull-out tests and the results were shown in inset of Fig.3A-E. The adhesion strength of rGO/FEVE nanocomposite coating firstly increased and then decreased with increasing in content of PS-PVP@rGO. When doping content of PS-PVP@rGO was about 1.0wt%, it showed largest adhesion strength (ca.14.0 MPa). The enhanced adhesion ability of rGO/FEVE nanocomposite coating was attributed to the incorporation of rGO nanosheets, effectively improving the mechanical strength of FEVE coating.

Fig.3.

The impact resistance of rGO/FEVE nanocomposite coating was evaluated by falling-weight tests and the results were shown in Fig.4. The hammer with a mass of 1000±1g was dropped from a certain height, and the impact resistance was determined by observing the damage of the coating surface (Fig.4A). The impact strength of the coatings was expressed by the product of impact height and the mass of the weight. As shown in Fig.4B, the pristine FEVE coating possessed a low impact resistance of *ca.* 6.86J. In contrast, after the addition of PS-PVP@rGO, the impact resistance of composite coating was greatly improved to 9.31 J. The enhanced impact resistance of composite coating was attributed to the reinforcing effect and good dispersion of rGO, agreeing well with the results obtained from adhesion tests. When the content of PS-PVP@rGO was further increasing to 2.5 wt%, the impact resistance dropped sharply below 6 J due to the incompatibility between PS and FEVE. These results further confirmed that mechanical properties of FEVE coating could be effectively improved by the introduction of PS-PVP@rGO.

Fig.4.

Fig.5 shows the polarization curves of the iron plate covered with different composite coatings. The fitted results of polarization curves were listed in Table 1. It was found that the I_{corr} values of surface-coated plate specimens were lower than that of bare iron. In addition, the I_{corr} of rGO/FEVE coated metal firstly decreased and then increased with increasing in content of PS-PVP@rGO. Among them, the rGO/FEVE coating with content of 1.5 wt% displayed the smallest I_{corr} of *ca.* 7.6×10^{-12}A/cm^2. The V_{corr} value of rGO/FEVE coated metal gradually decreased from 1.8×10^{-3} to 8.8×10^{-8} mm/year with increasing in content from 0 to 1.5 wt%. The I_{corr} and V_{corr} of rGO/FEVE coated metal were four or five order of magnitude lower than that of pure FEVE coated metal. As well-known, the nanocomposite coatings with lower I_{corr} show the better corrosion resistance [23]. This result was attributed to the good dispersion of PS-PVP@rGO in the FEVE matrix, resulting in higher polarization resistance (R_P) and better barrier property.

Fig.5.

Fig.6A shows the Nyquist plots of the bare metal plate and the surface-coated samples in 3.5 wt% NaCl aqueous solution. In this experiment, a larger semicircle represents a higher *Rct* value, indicating a long path of the ion diffusion from aqueous solution to metal substrate[24]. It clearly showed that the *Rct* value of the bare metal was far smaller than that of the surface-coated sample. The *Rct* value (*ca.* 229.9KΩ·cm^2) of metal coated with rGO/FEVE (1.5 wt%) was three orders of magnitude higher than that of the bare metal (*ca.* 0.145KΩ·cm^2) and almost three times that of the FEVE coated metal (67.9KΩ·cm^2). The superior performance of rGO/FEVE was attributed to the good barrier effect of dispersed rGO which reduced the permeability for corrosive substances. When the content of PS-PVP@rGO was further increased to 2.0 wt%, the *Rct* decreased, resulting from more cracks. Bode plot of the samples immersed in 3.5wt% NaCl aqueous solution was showed in Fig.6B. We found that the impedance value of the rGO/FEVE was higher than that of pure FEVE coating, indicating less possibility of corrosion. The result further confirmed the formation of rGO/FEVE with good anti-corrosion performance.

Fig.6.

Table1.

Salt spray test was carried out as a qualitative method to visually inspect the corrosion resistance of the coatings. The images of rGO/FEVE coated iron plates before and after subjecting to this test at different exposure time were presented in Fig.7A. After 120 days exposure, some blisters were observed. The corrosion process was extended under the scratched area in rGO/FEVE with various contents of 0, 0.5, 1.0 and 2.0 wt%. We also found some rusts along the scratched regions. The rGO/FEVE with content of 1.5 wt% was free from blisters and no rusts were observed along the scratched regions. Fig.7B shows the macroscopic surface images of the sample immersed in 3.5 wt% NaCl aqueous solution for 15 days. For pristine FEVE coating, a corrosion pit was observed on its surface and the color of polymer coating was changed at several sites. In contrast, there was no corrosion pit observed for the rGO/FEVE. These results further demonstrated the enhanced corrosion resistance of the rGO/FEVE.

Fig.7.

To determine the mechanism of excellent corrosion resistance, compatibility of FEVE and PS blend was simulated by molecular dynamics (MD) and mesoscopic dynamics (Meso Dyn). Firstly, density and solubility parameters (δ) of pure substances and Flory-Huggins (χ) interaction parameters of them were calculated by MD simulations with the COMPASS force field, experimental values for solubility parameters and density of pure substances were also given for comparing (as is shown in Table 2). PCTFE, PVE, PS and PVP represented the polytrifluorochloroethylene, polyvinyl ether, polystyrene, and polyvinylpyrrolidone, respectively. Finally, Flory-Huggins (χ) interaction parameters calculated from MD simulations were converted into Meso Dyn input parameters to predict properties of FEVE/PS blends.

Table 2.

According to the data in Table 2, the Flory-Huggins parameter χij and interaction energy between different polymer structural units can be obtained according to the formulas (1) and (2).

$$\chi_{ij} = V_r(\delta_i - \delta_j)^2/RT \qquad (1)$$

$$v^{-1}\varepsilon_{ij} = \chi_{ij}RT \qquad (2)$$

In the above formula, $\boldsymbol{\delta_i}$ and $\boldsymbol{\delta_j}$ are the solubility parameters of components i and j respectively, $(J / cm^3)^{1/2}$; $\mathbf{V_r}$ is the reference volume (average of the molar volume of components i and j), cm^3/mol; R is the gas constant, 8.314 J/(mol·K); T is the temperature, K. In the mesoscopic simulation method, the real polymer chain must undergo a certain degree of coarse graining, that is, a Gaussian chain composed of beads is used instead. Each bead is composed of one or several polymer monomers, and all beads have the same volume. Determining how many repeating units make up a bead is the focus of the coarse-graining process, the length of the beads Gaussian chain (N_{Meso}) is one of the important parameters in the mesoscopic simulation. It is related to the polymerization degree and the limit characteristic ratio of the selected polymer:

$$N_{Meso}=N/C_n \qquad (3)$$

N is polymerization degree of the polymer; C_n is the limit characteristic ratio of the polymer chain. So, A, B, C and D represent the PCTFE, PVE, PS, and PVP respectively and the corresponding polymers can be coarsely granulated into $A_{33}B_{32}$, C $_{215}$, D$_{42}$. Coarse-grained model of blend was shown in Fig.8A. The size of the box used in the simulation is 32nm×32nm×32nm. All bead diffusion coefficients were set to 1.0×10^{-7} cm^2/s, the system noise parameter was 75.002, the compressible parameter was set to 10, and the simulated temperature was 298K. Considering the equilibrium time of the system, the simulation step size was set to 50 ns, the total number of steps was 4000 steps, and the total simulation time was 200 μs. The blending morphology and iso-density simulation diagrams were shown in Fig.8B. Firstly, a mesoscopic simulation was carried out to study the compatibility between PS and FEVE. The morphology of the blend and the compatibility could be predicted by analyzing surface of the density fields. It was found that when the PS and FEVE were blended, the degree of phase separation increases with the increase of the content of PS in the FEVE as shown in Fig.8B. The PS morphology in the FEVE was initially aggregated into a sphere, and the volume gradually increased with the increase of the content. In addition, the cross-section SEM images of nanocomposite coating were also characterized as shown in Fig.8C-D. There were some particles on the fracture surface of the coating, which can be attributed to phase separation of PS in the FEVE matrix, forming PS spheres. These results indicated the formation of self-stratifying PS/FEVE blend resulting from the phase separation of PS in FEVE matrix.

Fig.8.

When comparing the corrosion resistance of the presented nanocomposite coatings with the performance reported in previous literature, we found that the presented coating exhibited the lowest I_{corr} and V_{corr}, suggesting a superior anti-corrosion performance (Table 3). The result can be attributed to the uniform dispersion of rGO in FEVE matrix and the self-stratifying between PS and FEVE blend, promoting the formation of connected rGO network in polymer matrix as shown in Scheme 1B. The formation of connected rGO network played a key role in improving the barrier property of polymer coating and enhancing the anti-corrosion performance [9]. Due to poor dispersion of rGO or the incompatibility of PS and FEVE, it is difficult to form a connected rGO network in the polymer matrix if the rGO content is too low or too high[10-16]. In fact, considering the attached PS and PVP, the content of rGO in FEVE matrix was only 0.22 wt% in the case of 2.0 wt% PS-PVP@rGO loading. The air film between hydrophobic surface and the surrounding water formed an additional nonconductive barrier, which effectively retard the diffusion process of ion and oxygen in water.

Table 3.

Scheme 1.

4. Conclusions

In this work, a novel rGO/FEVE nanocomposite coating was developed for application in anti-corrosion. The PS-PVP@rGO nanosheets could be directly dispersed in FEVE matrix due to its good re-dispersibility in xylene solution. The resulting nanocomposite coatings exhibited good mechanical properties and corrosion resistance, especially for the doping content of 1.5wt%. The result was attributed to synergistic effect of barriers of graphene and phase separation of PS. This research thus provides a new avenue to green preparation of nanocomposite coating based on rGO for improving anti-corrosion performance.

Acknowledgments

Luyan Shen and He Chen contributed equally to this work. The authors are grateful for the support of the National Natural Science Foundation of China under grants (51773184 and U1810114), Shanxi Provincial Natural Science Foundation of China (201803D421081 and 20181102014).

Conflict of interest

The authors declared that they have no conflicts of interest to this work.

Reference

[1]S. Zor, N. Ilmiev, Corrosion behavior of PANI/Epoxy/nano SnO_2 polymeric nanocomposite coated stainless steel in 3.5 wt% NaCl, Polymer composites, 39(2018)E2415-E2425.

[2]S.Bera, T.K. Rout, G. Udayabhanu, R. Narayan, Water-based & eco-friendly epoxy-silane hybrid coating for enhanced corrosion protection & adhesion on galvanized steel, Progress in Organic Coatings, 101 (2016) 24-44.

[3] X.Wang, Y.Li, C.Li, X.Zhang, D.Lin, F.Xu,Y.Zhu, H.Wang, J.Gong, T.Wang, Highly orientated graphene/epoxy coating with exceptional anti-corrosion performance for harsh oxygen environments, Corrosion Science,176(2020)109049.

[4]Y. K.Xiao, W.F.Ji, K.S.Chang, K.T.Hsu, J. M.Yeh, W. R.Liu, Sandwich-structured rGO/PVDF/PU multilayer coatings for anti-corrosion application, RSC Advances, 7 (2017) 33829-33836.

[5]A.Bordbar-Khiabani, S. Ebrahimi, B. Yarmand, Highly corrosion protection properties of plasma electrolytic oxidized titanium using rGO nanosheets, Applied Surface Science, 486 (2019) 153-165.

[6]C.Zhou, M.Hong, Y.Yang, N.Hu, Z.Zhou, L.Zhang, Y.Zhang, Engineering sulfonated polyaniline molecules on reduced graphene oxide nanosheets for high-performance corrosion protective coatings, Applied Surface Science, 484 (2019) 663-675.

[7]J. Li, J.Cui, J.Yang, Y.Li, H.Qiu, J.Yang, Reinforcement of graphene and its derivatives on the anticorrosive properties of waterborne polyurethane coatings, Composites Science and Technology, 129 (2016) 30-37.

[8]Y. Hu, Z. Chen, C. Wu, F. Wang, S. Cui, S. Ai, Y. Yang, The Synthesis and Research of Glass Fiber Felts Coated with Graphene Oxide/Phenolic Resin Binder, Fibers and Polymers, 20 (2019) 732-738.

[9]Y.Y.Zhou, Y.B.Ma, X.L.Li, C.Bian, Z.Y.Xiong, Y.Y.Sun, H.Chen, L.Y.Shen, Tunable rGO network in polymer coating for enhancing barrier property, Materials Research Bulletin,122(2020)110648.

[10]Z.Y.Zhang, W.H.Zhang, D.S.Li, Y.Y.Sun, Z.Wang, C.L.Hou, L.Chen, Y.Cao, Y.Q.Liu, Mechanical and Anticorrosive Properties of Graphene/Epoxy Resin Composites Coating Prepared by in-Situ Method, International Journal of Molecular Science, 16(2015)2239-2251.

[11]Y.Cao, X.Y.Tian, Y.Wang, Y.Y.Sun, H.L.Yu, D.S.Li, Y.Q.Liu, In Situ Synthesis of Reduced Graphene Oxide-Reinforced Silicone-Acrylate Resin Composite Films Applied in Erosion Resistance, Journal of Nanomaterials,2015,405087.

[12]Y.Wang, Y.Y.Zhou, Y.B.Ma, H.B.Lu, Y.Y.Sun, G.Z.Zhao, Y.Q. Liu, Preparation of a Natural Rubber Nanocomposite Coating based on Fe_3O_4@Carbon materials and their Corrosion Resistance, International of Journal of electrochemical Science,12(2017)9798-9811.

[13]J.G.Wen, W.M.Geng, H.Z.Geng, H.Zhao, L.C.Jing, X.T.Yuan, Y.Tian, T.Wang, Y.J.Ning, L.Wu, Improvement of Corrosion Resistance of Waterborne Polyurethane Coatings by Covalent and Noncovalent Grafted Graphene Oxide Nanosheets, ACS OMEGA, 4(2019)20265-20274.

[14]M.R. Ghadimi, A. Dolati, Preparation and characterization of superhydrophobic and highly oleophobic FEVE-SiO_2 nanocomposite coatings, Progress in Organic Coatings, 138 (2020) 105388.

[15]R. Yuan, H. Liu, Y. Chen, Z. Liu, Z. Li, J. Wang, G. Jing, Y. Zhu, P. Yu, H. Wang, Design ambient-curable superhydrophobic/electroactive coating toward durable pitting corrosion resistance, Chemical Engineering Journal, 374 (2019) 840-851.

[16]R.G. Song, L. Chen, H. Lu, Effects of nanoparticles on the corrosion resistance of fluoropolymer coatings on mild steel, Surface Engineering, 33 (2016) 451-459.

[17]Y. Zhou, Y. Ma, Y. Sun, Z. Xiong, C. Qi, Y. Zhang, Y. Liu, Robust Superhydrophobic Surface Based on Multiple Hybrid Coatings for Application in Corrosion Protection, ACS applied materials & interfaces, 11 (2019) 6512-6526.

[18]JS.Cui, SX.Zhou, Polyamine-functionalized perylene bisimide for dispersion of graphene in water with high effectiveness and little impact on electrical conductivity, Journal of Nanoparticle Research, 19(2017)357.

[19]R. Khaledialidusti, E. Mahdavi, A. Barnoush, Stabilization of 2D graphene, functionalized graphene, and Ti_2CO_2 (MXene) in super-critical CO_2: a molecular dynamics study, Physical Chemistry Chemical Physics, 21(2019)12968-12976.

[20]A.M. Abdelghany, M.S. Mekhail, E.M. Abdelrazek, M.M. Aboud, Combined DFT/FTIR structural studies of monodispersed PVP/Gold and silver nano particles, Journal of Alloys and Compounds, 646 (2015) 326-332.

[21]Y.H. Yu, Y.Y. Lin, C.H. Lin, C.C. Chan, Y.C. Huang, High-performance polystyrene/graphene-based nanocomposites with excellent anti-corrosion properties, Polym. Chem., 5 (2014) 535-550.

[22] D. Kumar, L. Li, Z. Chen, Mechanically robust polyvinylidene fluoride (PVDF) based superhydrophobic coatings for self-cleaning applications, Progress in Organic Coatings, 101 (2016) 385-390.

[23]Y. Qing, C. Yang, N. Yu, Y. Shang, Y. Sun, L. Wang, C. Liu, Superhydrophobic TiO_2/polyvinylidene fluoride composite surface with reversible wettability switching and corrosion resistance, Chemical Engineering Journal, 290 (2016) 37-44.

[24] J. Yang, J. Li, X. Jia, Y. Li, and H. Song, Fabrication of Robust and Transparent Slippery Coating with Hot Water Repellency, Antifouling Property, and Corrosion Resistance,ACS Appl. Mater. Interfaces,12(2020) 28645-28654.

[25]H.Di, Z.Yu, Y.Ma, C.Zhang, F.Li, L. Lv, Y. Pan, H. Shi, Y. He, Corrosion-resistant hybrid coatings based on graphene oxide–zirconia dioxide/epoxy system, Journal of the Taiwan Institute of Chemical Engineers, 67 (2016) 511-520.

[26]Y.T. Lin, T.M. Don, C.J. Wong, F.C. Meng, Y.J. Lin, S.Y. Lee, C.F. Lee, W.Y. Chiu, Improvement of mechanical properties and anticorrosion performance of epoxy coatings by the introduction of polyaniline/graphene composite, Surface and Coatings Technology, 374 (2019) 1128-1138.

[27]G. Jiang, X. Li, Y. Che, Y. Lv, F. Liu, Y. Wang, C. Zhao, X. Wang, Antibacterial

and anticorrosive properties of CuZnO@RGO waterborne polyurethane coating in circulating cooling water, Environ Sci Pollut Res Int, 26 (2019) 9027-9040.

[28]S.Teng, Y.Gao, F. Cao, D. Kong, X. Zheng, X. Ma, L. Zhi, Zinc-reduced graphene oxide for enhanced corrosion protection of zinc-rich epoxy coatings, Progress in Organic Coatings, 123 (2018) 185-189.

[29] C.Chen, Y.He, G.Xiao, Y.Xia, H.Li, Z.He, Two-dimensional hybrid materials: MoS_2-RGO nanocomposites enhanced the barrier properties of epoxy coating, Applied Surface Science, 444 (2018) 511-521.

[30]K.Cai, S.Zuo, S.Luo, C.Yao, W.Liu, J.Ma, H.Mao, Z.Li, Preparation of polyaniline/graphene composites with excellent anti-corrosion properties and their application in waterborne polyurethane anticorrosive coatings, RSC Adv., 6 (2016) 95965-95972.

[31]W.Sun, L.Wang, T. Wu, Y. Pan, G. Liu, Synthesis of low-electrical-conductivity graphene/pernigraniline composites and their application in corrosion protection, Carbon, 79 (2014) 605-614.

[32]X.Sheng, W.Cai, L.Zhong, D.Xie, X.Zhang, Synthesis of Functionalized Graphene/Polyaniline Nanocomposites with Effective Synergistic Reinforcement on Anticorrosion, Industrial & Engineering Chemistry Research, 55 (2016) 8576-8585.

[33] T.R. Tamilarasan, U. Sanjith, M. Siva Shankar, G. Rajagopal, Effect of reduced graphene oxide (rGO) on corrosion and erosion-corrosion behaviour of electroless Ni-P coatings, Wear, 390-391 (2017) 385-391.

[34]K.Zhu, X.Li, H. Wang, J. Li, G. Fei, Electrochemical and anti-corrosion behaviors of water dispersible graphene/acrylic modified alkyd resin latex composites coated carbon steel, Journal of Applied Polymer Science, 134 (2017).

Table1.Analysis results of Tafel Polarization Curves and Electrochemical Impedance Spectroscopy of composite coatings with different contents.

Table 2. Properties of pure polymers evaluated by molecular dynamics

Table 3. Anti-corrosion performance of polymer nanocomposite coating based on rGO

Scheme 1. Schematic illustration of protection mechanisms of (A)rGO/polymer coating and (B)Self-stratifying PS@rGO/polymer coating.

Fig.1. (A)FT-IR spectra of (a) rGO, PS-PVP@rGO (b) before and (c)after dispersing in xylene, (B)Raman spectrum of PS-PVP@rGO, SEM images of (C) rGO and (D) PS-PVP@rGO, TEM images of (E) rGO and (F) PS-PVP@rGO. The inset of B is the optical photograph of dry PS-PVP@rGO dispersed in xylene.

Fig.2.SEM images of rGO/FEVE with various PS-PVP@rGO contents of (A)0, (B)0.5wt%, (C)1.0wt%, (D)1.5wt% and (E)2.0wt%. The inset of A is the optical microscopy photograph of rGO/FEVE coated on surface of metal.

Fig.3.Optical photographs of rGO/FEVE nanocomposite coatings after knife-scratch, (A)0, (B)0.5wt%, (C)1.0wt%, (D)1.5wt% and (E)2.0wt%. The corresponding insets are optical photographs of pull-off tests.

Fig.4. (A)Optical photographs and (B)impact strength of rGO/FEVE nanocomposite coatings by falling weight test. (a)0, (b)0.5wt%, (c)1.0wt%, (d)1.5wt% and (e)2.0wt%.

Fig.5. Tafel polarization curves of rGO/FEVE nanocomposite coatings in 3.5wt% NaCl aqueous solution. (A)0, (B)0.5wt%, (C)1.0wt%, (D)1.5wt% and (E)2.0wt%.

Fig.6.(A)Nyquist plots and (B)Bode plots of |Z| vs frequency of rGO/FEVE nanocomposite coatings with different contents of (a)0, (b)0.5wt%, (c)1.0wt%, (d)1.5wt% and (e)2.0wt%. The inset of A is Nyquist plots of bare Fe.

Fig.7. Optical photographs of coated-Fe samples exposed to (A)NaCl 5.0wt% fog and (B) 3.5wt% NaCl aqueous solution for 120 days and 15 days, respectively.

Fig.8. (A)Coarse granulation model of polymer blend system (blue、green and red represent PS、FEVE matrix and PVP respectively), (B)Blending morphology and iso-density simulation diagrams of FEVE with different PS and PVP contents of (a)1.0wt%、0.05wt%, (b)3.0wt%、0.15wt%, (c)10.0wt%、0.5wt% and (d)50.0wt%、2.5wt%. Cross-section SEM images of PS/FEVE nanocomposite coatings with various PS contents of (C)1.0wt% and (D)3.0wt%.

Table 1.

Samples	E_{corr} (V)	I_{corr} ($A\cdot cm^{-2}$)	V_{corr} (mm/year)	R_p ($M\Omega\cdot cm^2$)	Rct ($K\Omega\cdot cm^2$)
Steel	-1.04	3.2×10^{-4}	3.68	3.1×10^{-2}	0.145
FEVE	-0.73	1.6×10^{-7}	1.8×10^{-3}	16.3	67.9
0.5wt%	-0.60	7.0×10^{-10}	8.1×10^{-6}	1.6×10^{5}	76.1
1.0wt%	-0.42	4.6×10^{-11}	5.4×10^{-7}	4.5×10^{5}	180.7
1.5wt%	-0.31	7.6×10^{-12}	8.8×10^{-8}	6.6×10^{6}	229.9
2.0wt%	-0.46	8.8×10^{-9}	1.0×10^{-4}	2.4×10^{4}	116.1

Table 2.

component	$\delta(J/cm^3)^{1/2}$		$\rho(g/cm^3)$		$M_m(g/cm^3)$	V_m (cm^3/mol)
	Literature	simulation	Literature	simulation		
PS	15.6~21	15.7	1.05	1.00	104	104.00
PVP	-	17.3	1.14	1.01	97	96.03
PCTFE	14.7~16.2	15.1	2.12~2.16	1.95	116.5	59.74
PVE	-	15.0	0.96	0.94	70	74.47

Table 3.

Samples	E_{corr} (V)	I_{corr} (A cm^{-2})	V_{corr} (mm/year)	R_p (MΩ cm^2)	Reference
rGO/FEVE	-0.31	7.6×10^{-12}	8.83×10^{-8}	6.6×10^{6}	Present work
SPANI-rGO/EP	-0.23	3.31×10^{-6}	/	/	[10]
rGO/EP	-0.20	3.70×10^{-9}	4.30×10^{-5}	/	[13]
GNS/EP	-0.96	1.8×10^{-7}	0.3	/	[14]
rGO/SAR	-0.59	4.5×10^{-7}	0.8	/	[15]
Fe_3O_4@rGO/NR	-0.27	1.40×10^{-6}	1.6×10^{-2}	/	[16]
PANI/rGO/EP	-1.04	5.19×10^{-9}	1.21×10^{-8}	5.5×10^{-5}	[26]
CuZnO@RGO/ WPU	-0.60	7.0×10^{-4}	0.01	/	[27]
Zn-rGO/ZRC	-0.54	6.33×10^{-8}	/	0.7	[28]
MoS_2-RGO/EP	-0.46	1.8×10^{-3}	/	1.46×10^{-2}	[29]
RGO/PANI/WPU	-0.35	3.69×10^{-10}	4.3×10^{-6}	3.06	[30]
rGO	-0.13	7.18×10^{-9}	8.38×10^{-5}	72.2	[31]
PGO/PANI	-0.28	7.32×10^{-9}	1.68×10^{-4}	2.37	[32]
Ni-P-rGO	-0.31	1.42×10^{-6}	/	/	[33]
PG/AMAR	-0.18	2.85×10^{-8}	3.31×10^{-4}	1.13×10^{2}	[34]

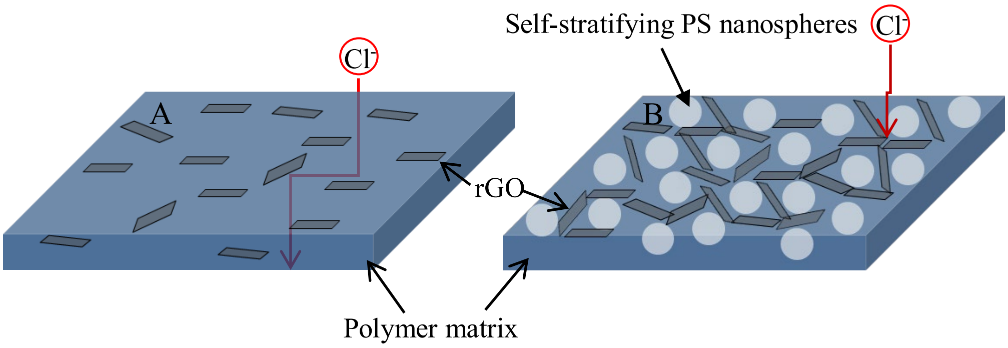
Self-stratifying PS nanospheres
Cl⁻
Cl⁻
A
B
rGO
Polymer matrix

Scheme 1.

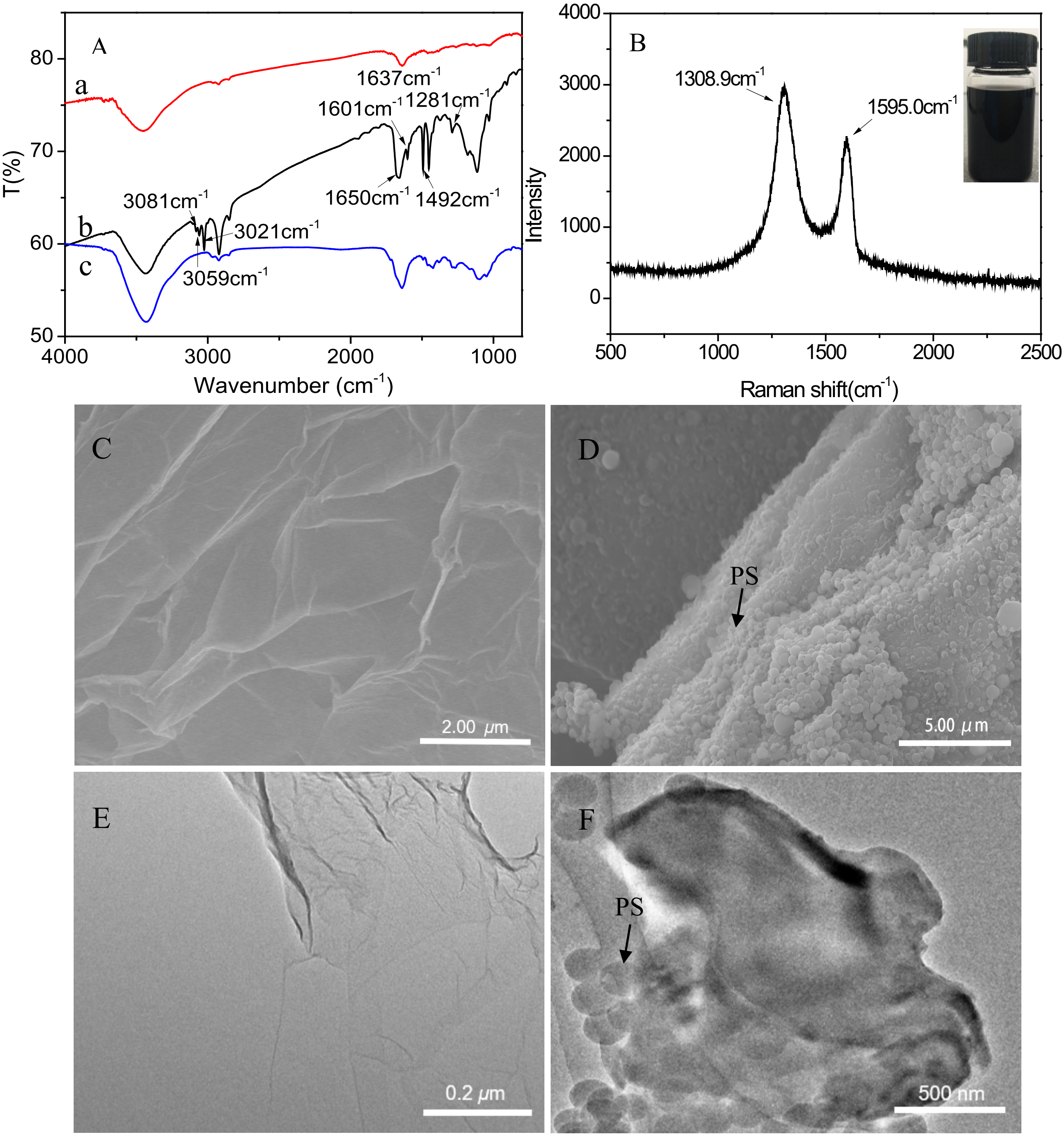
A
a
b
c
80
70
60
50
T(%)
4000
3000
2000
1000
Wavenumber (cm-1)
1637cm-1
1601cm-1
1281cm-1
1650cm-1
1492cm-1
3081cm-1
3021cm-1
3059cm-1
B
4000
3000
2000
1000
0
Intensity
500
1000
1500
2000
2500
Raman shift(cm-1)
1308.9cm-1
1595.0cm-1
C
2.00 μm
D
PS
5.00 μm
E
0.2 μm
F
PS
500 nm

Fig.1.

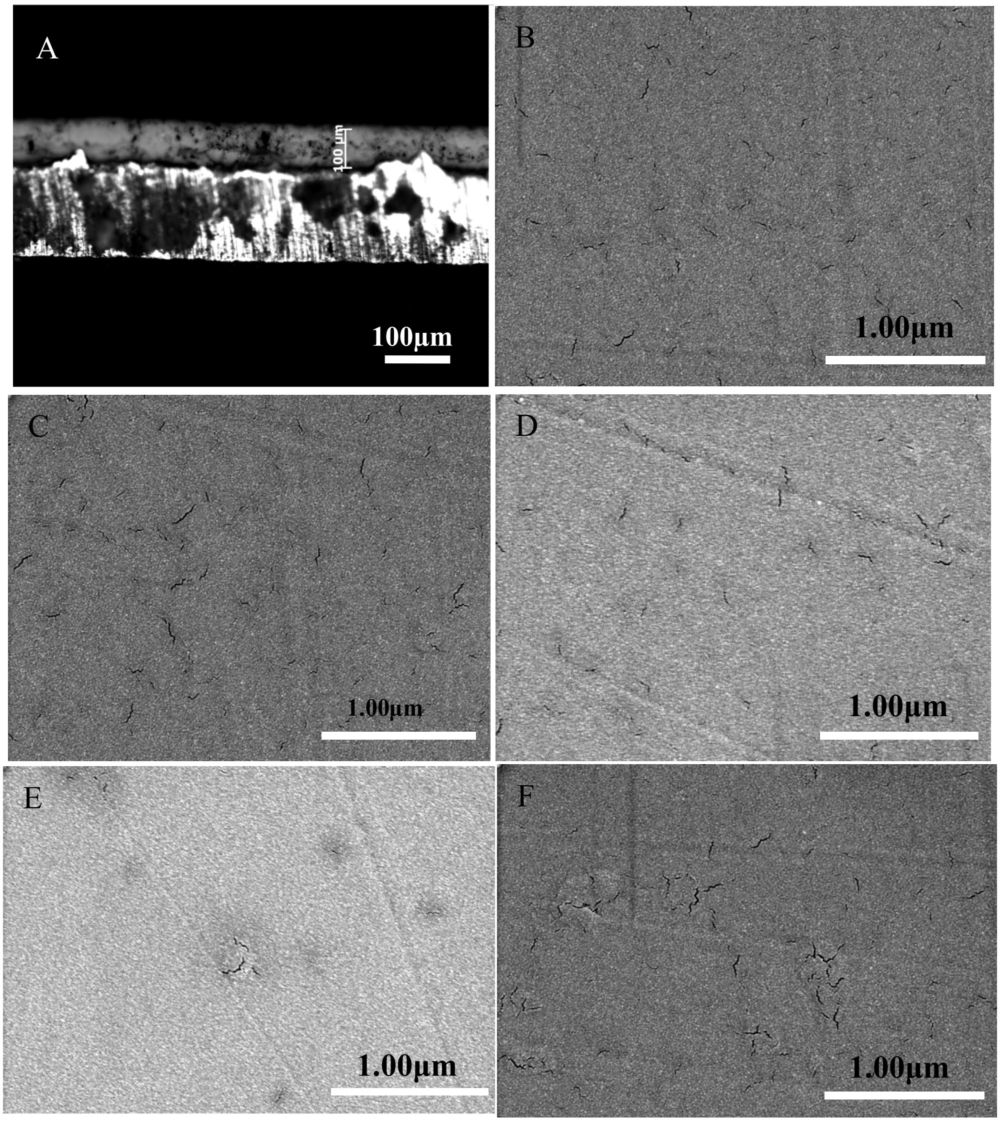

Fig.2.

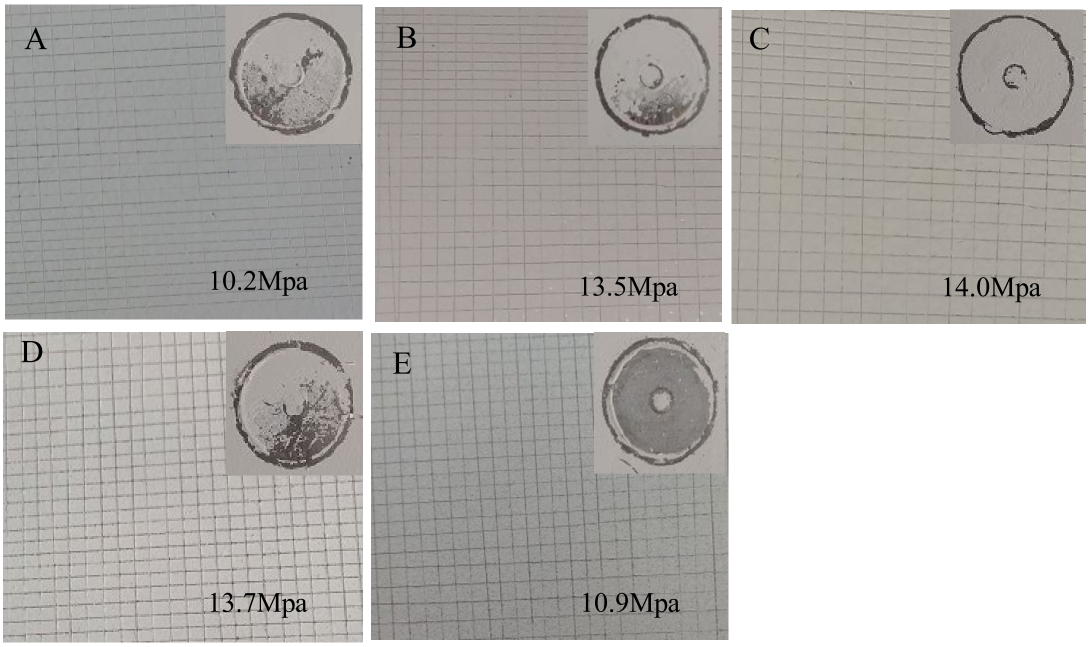

Fig.3.

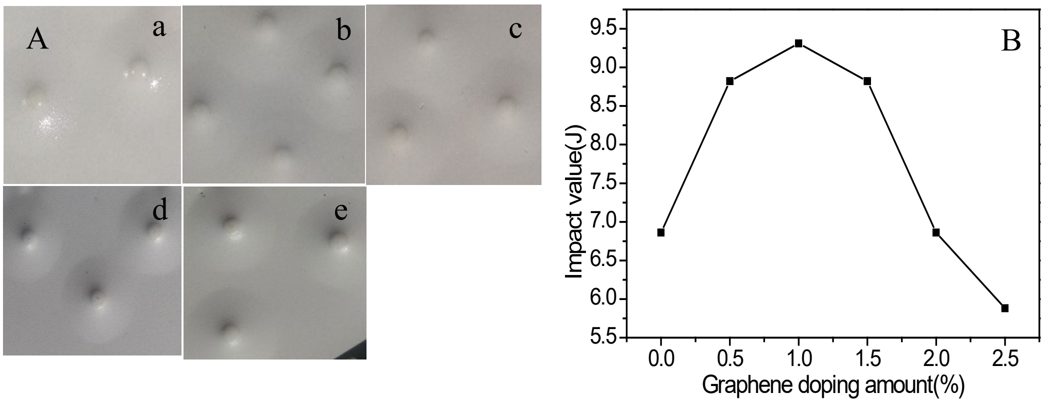
A
a
b
c
d
e
B
Impact value(J)
9.5
9.0
8.5
8.0
7.5
7.0
6.5
6.0
5.5
0.0
0.5
1.0
1.5
2.0
2.5
Graphene doping amount(%)

Fig.4.

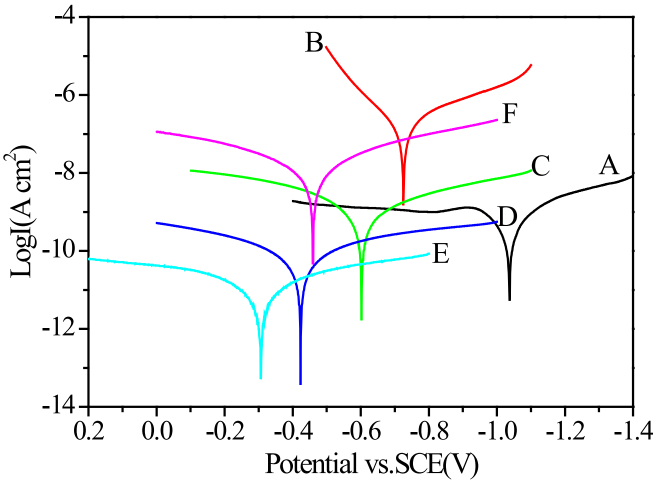
LogI(A cm^2)
-4
-6
-8
-10
-12
-14
0.2
0.0
-0.2
-0.4
-0.6
-0.8
-1.0
-1.2
-1.4
Potential vs.SCE(V)
B
F
C
A
D
E

Fig.5.

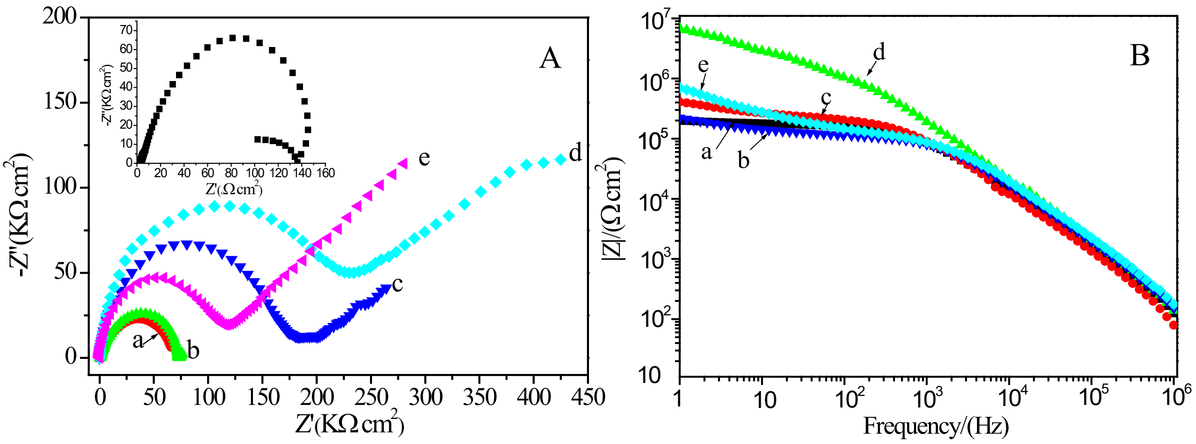
A
-Z''(KΩcm^2)
Z'(KΩcm^2)
0
50
100
150
200
250
300
350
400
450
-Z''(KΩcm^2)
Z'(Ωcm^2)
0
10
20
30
40
50
60
70
20
40
60
80
100
120
140
160
a
b
c
d
e
B
|Z|/(Ωcm^2)
Frequency/(Hz)
10
10^2
10^3
10^4
10^5
10^6
10^7
1
a
b
c
d
e

Fig.6.

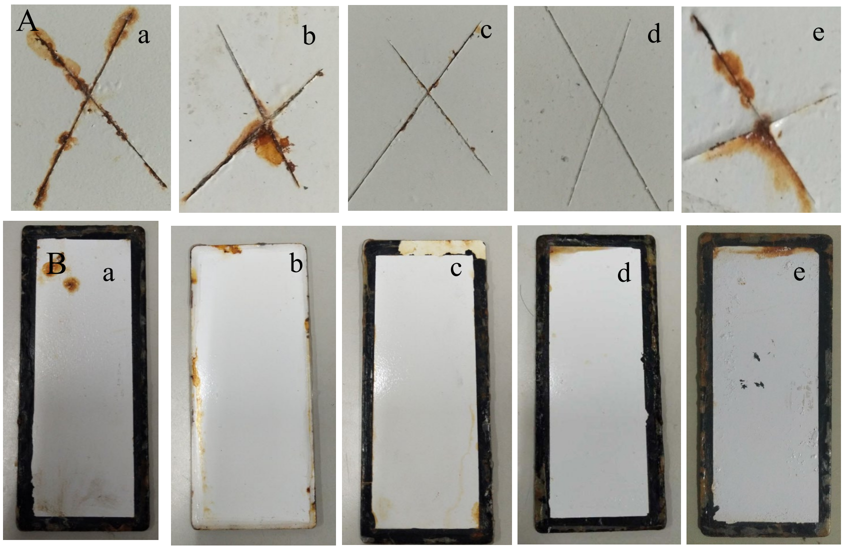
A
a
b
c
d
e
B
a
b
c
d
e

Fig.7.

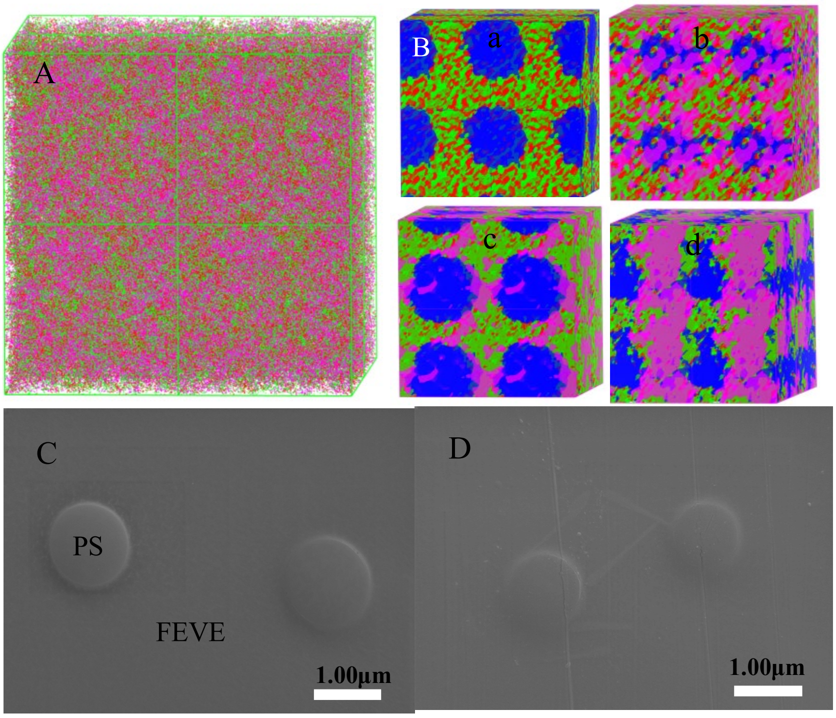

Fig.8.